

# **Evaluation of post-tensioned reinforced and fiber reinforced concrete beams by using DOFS**

Downloaded from: https://research.chalmers.se, 2025-11-29 01:34 UTC

Citation for the original published paper (version of record):

Fernandez, I., Ekstrom, D., Rempling, R. et al (2025). Evaluation of post-tensioned reinforced and fiber reinforced concrete beams by using DOFS. Structural Concrete, 26(5): 6274-6293. http://dx.doi.org/10.1002/suco.70224

N.B. When citing this work, cite the original published paper.

research.chalmers.se offers the possibility of retrieving research publications produced at Chalmers University of Technology. It covers all kind of research output: articles, dissertations, conference papers, reports etc. since 2004. research.chalmers.se is administrated and maintained by Chalmers Library

### ARTICLE



# **Evaluation of post-tensioned reinforced and fiber** reinforced concrete beams by using DOFS

Ignasi Fernandez<sup>1</sup> | Daniel Ekström<sup>2</sup> | Rasmus Rempling<sup>3,4</sup> | Carlos G. Berrocal<sup>1</sup>

<sup>1</sup>Division of Structural Engineering, Chalmers University of Technology, Göteborg, Sweden

<sup>2</sup>Division of Bridge and Hydraulic Design, WSP Sverige AB, Gothenburg, Sweden

<sup>3</sup>Division of Construction Management and Engineering, Chalmers University of Technology, Göteborg, Sweden

<sup>4</sup>Division of R&D, NCC Sverige AB, Göteborg, Sweden

### Correspondence

Ignasi Fernandez, Division of Structural Engineering, Chalmers University of Technology, Göteborg, SE-41296, Sweden. Email: ignasi.fernandez@chalmers.se

## **Funding information**

SBUF: Svenska Byggbranschens Utvecklingsfond, Grant/Award Number: SBUF- 14134

### Abstract

Prestressed concrete provides several advantages over traditional reinforced concrete; however, some markets remain skeptical about the use of posttensioned structures. A crucial factor in these structures is assessing and quantifying the final force introduced into the element. This study evaluates the application of distributed optical fiber sensors (DOFS) to monitor the response of beams during tendon force introduction, long-term behavior, and loading to failure. An experimental campaign was conducted involving four beams: two standard and two post-tensioned. Additionally, the study compares the effectiveness of steel fiber reinforced concrete to determine its potential for further optimizing beam design. Key aspects analyzed include tendon force and corresponding instantaneous and deferred losses, load-deformation behavior, initial crack formation, and subsequent crack development. The results demonstrated that using DOFS in a straightforward manner allows for detailed beam response analysis across different phases. Simple hypotheses and limited sensors can accurately evaluate all tendon losses. Furthermore, fiber optics can detect potential crack candidates even in the compression stage, due to strain concentrations that lead to cracking during the loading phase.

### KEYWORDS

crack monitoring, distributed optical fiber sensing, fiber optics, post-tensioned concrete, post-tensioning loses, steel fiber reinforced concrete

# 1 | INTRODUCTION

Prestressed concrete, especially post-tensioned reinforced concrete (PRC), provides several benefits compared to traditional reinforced concrete, such as improved crack control, reduced deflections, the ability for longer spans, as well as a more efficient use of materials. Prestressed concrete has been utilized in many civil engineering projects worldwide since its introduction in the 1940s. The

application of PRC includes, among others, large road and railway bridges, nuclear reactors, storage tanks, silos, building floors, and wind turbine foundations. In Sweden, approximately 20% of the over 2500 bridges maintained by The Swedish Transport Administration use post-tensioning technology.

The structural performance and durability of PRC systems are predominantly influenced by the initial posttensioning forces in the tendons and their condition over

This is an open access article under the terms of the Creative Commons Attribution License, which permits use, distribution and reproduction in any medium, provided the original work is properly cited.

© 2025 The Author(s). Structural Concrete published by John Wiley & Sons Ltd on behalf of International Federation for Structural Concrete.



17317464, 2025, 5, Downloaded from https://onlinelibrary.wiley.com/doi/10.1002/suco.70224 by Statens Beredning, Wiley Online Library on [24/11/2025]. See the Terms and Conditions (https://onlinelibrary.wiley.com/emm-and-conditions) on Wiley Online Library for rules of use; OA articles are governed by the applicable Creative Commons Licenses

the structure's service life. Furthermore, it is common that existing PRC structures show signs of deterioration, and estimating the residual prestressing force in posttensioned structures has become increasingly important.<sup>1</sup> However, the evaluation of this force may prove challenging, primarily due to uncertainties related to the magnitude and distribution of prestress losses over time.<sup>2</sup> Precise estimation of these forces is crucial for maintaining structural integrity, ensuring safety, and extending the serviceability of these structures. Furthermore, monitoring the initiation and propagation of cracks is essential, as cracks can significantly accelerate tendon corrosion and other degradation mechanisms. To address these challenges, innovative monitoring techniques are critical for providing accurate, real-time data, fostering improved structural assessments, and enhancing confidence in PRC technologies. As detailed in References [3,4] several methods are commonly used to this end, exhibiting different benefits and drawbacks, although a common conclusion is that strain-based alternatives represent the highest potential.

In this regard, the use of advanced strain-monitoring techniques, such as distributed optical fiber sensors (DOFS), applied to these components can lead to new insights and a deeper understanding of their structural performance, as seen in recent works applied to different types of structures. DOFS offer multiple benefits over conventional sensors, including compact size, lightness, resistance to chemical and corrosion degradation, and electromagnetic interference immunity. With recent advancements in optical Rayleigh backscattering reflectometry, there has been a leap forward in the capability to continuously monitor strain along fiber cables with eligible spatial resolutions that span from half centimeter to up to the sub-millimeter scale, depending on the application,<sup>5</sup> providing new options for performance evaluation. This technology has already been effectively employed in a wide range of civil engineering projects,6 such as monitoring of tunnel infrastructure,7,8 concrete bridges, 4,9 and monitoring strain in reinforced concrete beams. 10-14 Furthermore, its effectiveness in supporting the validation of performance indicators for reinconcrete elements—specifically in deflection measurement and the identification, location, measurement of cracks and long-term applicability—has been extensively researched and proven. 15-18

Some attempts have also been made to monitor prestressed concrete elements using DOFS. Gao et al. 19 used Brillouin-based DOFS attached directly to prestressing strands to investigate how the tendon force varied along the length during the tensioning operation and subsequent four-point loading. The study concluded that DOFS could be used to obtain the stress distribution along the tendons, including anchorage losses, as well as

the long-term loss due to shrinkage and creep. However, the system used provided a spatial resolution of only 1 m, which is not enough to detect and monitor cracking. In, Reference [20] Lan and co-authors also used Brillouinbased DOFS to create a smart strand consisting of a straight optic fiber cable with 6 steel wires coiled around it. With the smart strand sensor, they were able to monitor the tensioning operation and the initial losses of a PRC beam, although the developed sensor exhibited significant noise even with a straight profile and the measurements lasted only 10 days. The same type of smart strand and test setup was used by Huynh and Kim<sup>21</sup> to study temperature effects on the prestressing force, although using Fiber Bragg Grating sensors instead, that is, only having discrete measurement points along the fiber. Webb et al.22 embedded Brillouin-based DOFS in several of the PRC beams of the Nine Wells Bridge in Cambridgeshire, UK. They monitored both strain and temperature during the tensioning operation as well as in service for a period of up to 1000 days. However, measurements were not continuous over time; namely, only 8 measurements in the entire period were performed, while some of the fibers were damaged during the execution of the bridge. Furthermore, Derkowski et al.<sup>23</sup> attached Rayleigh-based DOFS on the top surface of a 57-year-old beam with clear signs of deterioration to investigate the effect of losing the mechanical anchorage on the prestressing force in the bonded tendons. More recently, Piatek et al.24 successfully studied different DOFS sensors in post-tensioned beams to evaluate some global performance requirements. A later work by Piątek et al.<sup>25</sup> used DOFS for the evaluation of several parameters of post-tensioned elements; however, the remaining post-tensioning force was not evaluated.

Despite advancements in DOFS, critical questions remain regarding their practical deployment, effective monitoring of instantaneous and deferred tendon losses, and detailed crack detection under operational loads. For example, most of the existing literature focuses on non-Rayleigh DOFS technologies, which offer significant advantages in terms of sensor length per channel, suitable for very large infrastructure, but lack the resolution necessary for meaningful evaluations of crack opening and development or detailed evaluation of local phenomena. Conversely, existing studies utilizing Rayleighbackscattering technology involve more advanced and complex solutions such as smart tendons or FRP-based smart bars, also called monolithic sensors, rather than focusing on optimal configurations using off-the-shelf sensors. Additionally, this technology is constrained by limited sensor lengths per channel, which currently extend up to 100 meters per channel. This may present limitations in large bridges or multi-span configurations.

7517648, 2025, 5, Downloaded from https://onlinelibrary.wiley.com/doi/10.1002/suco.70224 by Statens Beredning, Wiley Online Library on [24/11/2025]. See the Terms and Conditions (https://onlinelibrary.wiley.com/terms

of use; OA articles are governed by the applicable Creative Commons License

Therefore, it is crucial to evaluate simple deployment setups with shorter sensor lengths to maximize the system's possibilities and reduce costs.

This study aims to explore the efficient implementation of DOFS for comprehensive performance monitoring of newly built prestressed reinforced concrete (PRC) structures from construction up to ultimate failure loading, including long-term service loading. Additionally, the research examines both conventional concrete and steel fiber reinforced concrete (SFRC), evaluating SFRC's effectiveness in enhancing structural performance. The findings suggest that employing DOFS in PRC/SFRC beams in a bilayer configuration (with only two sensors) is viable, providing valuable, high-resolution data throughout all structural phases, thereby significantly enhancing structural health monitoring capabilities and overall structural safety.

# 2 | EXPERIMENTAL PROGRAM

An experimental program was devised to explore how DOFS can accurately monitor the service and ultimate limit states of PRC and post-tensioned fiber reinforced concrete (PFRC) beams. To that end, two sets of beams, equipped with multi-layered DOFS configurations, were cast. Each set included one beam with post-tensioning tendons and another with only passive reinforcement. The primary distinction between the two sets was the concrete mix, namely a standard concrete mix and a fiber reinforced concrete mix. Both groups of specimens were

designed based on identical criteria, that is, maximum load to be resisted, crack opening, and maximum allowed deflection at service load. These noticeably led to differences in the final shape and featured reinforcing of each specimen due to the varying capacities of their respective individual components to meet these design parameters. A detailed geometrical description of the beam sets and the loading setup used is provided in the following.

# 2.1 | Geometry and reinforcement layout

The specimens used in this experimental work are shown in Figure 1, where a general view of one of the specimens is seen in the testing rig, and in Figures 2 and 3 were a detailed description of the geometry and elevation is shown for all the beams.

# 2.1.1 | Plain concrete specimens

The elements encompassed in this set of beams spanned a total length of 8.5 m, each with a T-shaped cross-section. The top of the T-section measured 320 mm in width and 130 mm in height, while the web was 515 mm tall and 150 mm wide, bringing the total height of each beam to 645 mm. One of the beams was labeled as "PRC," including both post-tensioning tendons and passive reinforcement. In contrast, the reference beam, labeled as the "RC" specimen, had only passive reinforcement. The PRC beam had three 16 mm diameter rebars



FIGURE 1 PRC before testing to failure and detail of the anchor system used for up to 5 tendons, note that in this work only 4 tendons were installed in both the PRC/PFRC specimens.

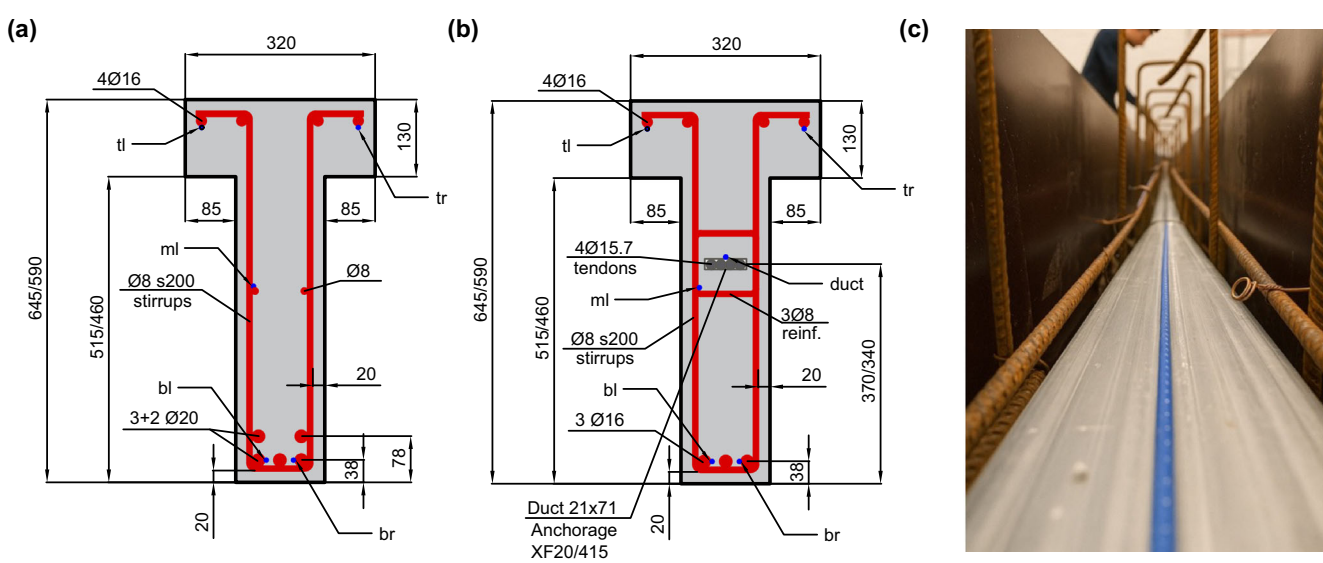
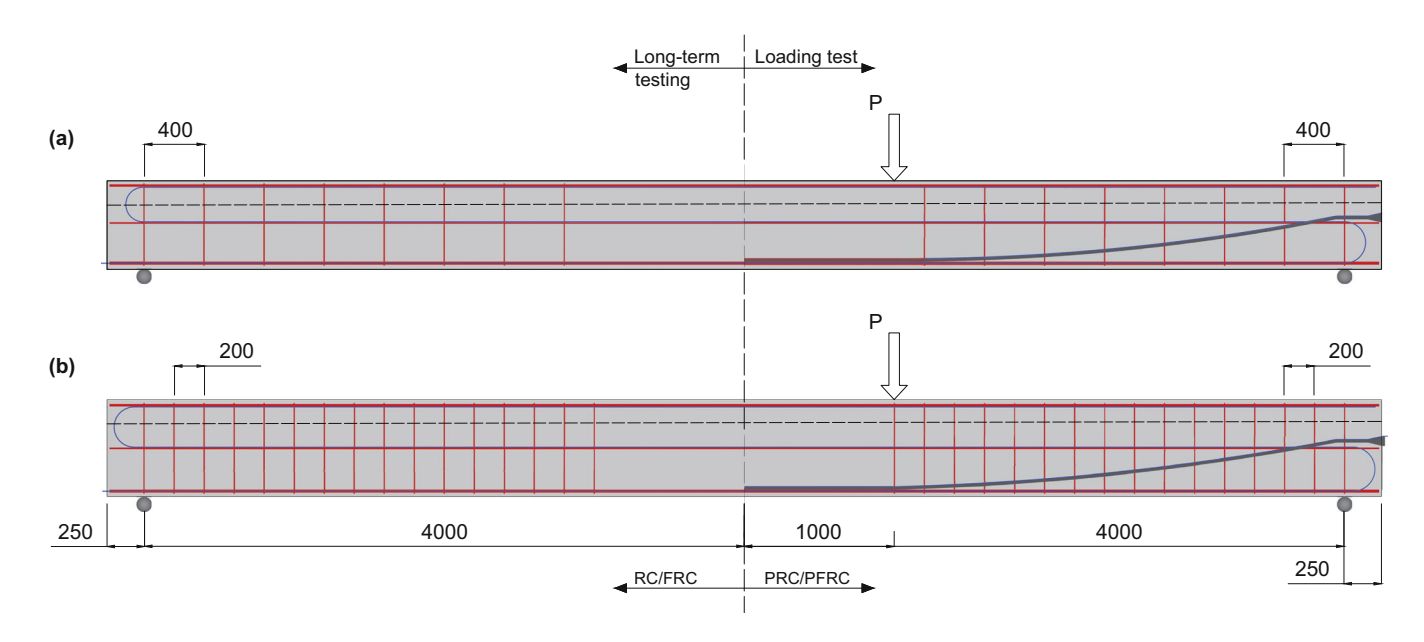


FIGURE 2 Geometry of the plain reinforced concrete and the post-tensioned specimens, reinforcement layout (all measurements in mm). (a) RC/FRC beam, (b) PRC/PFRC beam. The labeling of the FO cables indicated by "yx" follows the criteria where y points to the vertical position: "t" for top, "m" for middle, and "b" for bottom part of the section. The x indicates the position in the horizontal direction, with "l" for left and "r" for right position in the section. (c) FO installation on the duct of a PRC specimen.



Sensor deployment, reinforcement layout and test-setup. Setup for long-term testing is shown for beams without posttensioning (left) and setup for loading to failure is shown for beams with post-tensioning (right). Reinforcement layout (a) FRC/PFRC and (b) RC/PRC beam sets. The longitudinal arrangement of the sensor along the beam length is indicated by the blue lines while the red and gray lines correspond to the passive and active steel reinforcement respectively.

on the lower side and four on the upper side. It also featured a flat plastic duct measuring 71 × 21 mm internally, containing a total of four 15.7 mm diameter tendons, type Y1860S7 featuring a characteristic value of the tensile strength of 1860 MPa. The duct was arranged into a parabolic shape to enhance efficiency under the loading tests. The duct ran straight for about 250 mm from the beam ends before transitioning into a parabolic

curve for three meters, ultimately straightening in the final meter towards the center of the beam. The duct rested on top of the passive reinforcing bars and mirrored symmetrically about the mid-point of the beam.

A full CCL XF20/5/13 anchorage flat system used in civil engineering structures that connect individually tensioned bare strands through a plastic flat duct, see Figure 1, was used on both ends of the beam connecting

	Cube 1, [MPa]	Cube 2, [MPa]	Cube 3, [MPa]	Mean, [MPa]
RC/PRC	61.3	57.9	61.2	60.2
FRC/PFRC	67.2	65.5	69.3	67.3

**TABLE 1** Cube test results for RC/PRC and FRC/PFCR specimens.

the duct and enabling load introduction after casting. It is important to note that although the anchorage system has a capacity for up to five tendons, this study utilized only four tendons per beam. To resist shear stresses and prevent local failure at the anchorage system, transversal reinforcement was added: U-shaped 8 mm diameter open stirrups every 200 mm in the initial 3.5 m from both sides of the beam. and a squared stirrup around the force unit transfer. The RC specimen featured a similar layout of passive reinforcement, but without the duct, which was replaced with two extra 16 mm diameter bars positioned similarly. Unlike the PRC, these bars were placed completely straight from one end of the beam to the other. The reinforcement layouts for both specimens are illustrated in Figure 2a, b, respectively. The steel quality used for the passive reinforcement was B500B, according to the Eurocode, which has a characteristic yielding strength of 500 MPa.

A self-compacting concrete mix was used to cast the specimens, featuring a concrete strength class C40/50 and a water-to-cement ratio (w/c) of 0.40. The maximum aggregate size was 8 mm, and standard Portland cement was used. Following the casting, the specimens were covered with a polyethylene sheet to reduce moisture evaporation. The material compression test for 150 mm cubes is described in Table 1.

# 2.1.2 | Fiber-reinforced specimens

In line with the previous set, two beams were also cast: one designated "PFRC" with both active and passive reinforcements, and another labeled "FRC" containing only passive reinforcement. These beams maintained the same T-shaped cross-section. However, the addition of steel fibers in the concrete mix enabled decreasing the web height to 460 mm, resulting in an overall beam height of 590 mm, as depicted in Figure 2a, b. The arrangement of longitudinal steel reinforcement was kept consistent across the different sets. Yet, due to the shear resistance provided by the steel fibers mixed into the concrete, it was possible to halve the amount of shear reinforcement needed, leading to U-shaped stirrups being spaced at 400 mm, as shown in Figure 2a, b. The same anchorage system illustrated in Figure 1 was also employed for these beams. These specimens used the same concrete mixture, with the addition of 0.5% by cement weight of Dramix 65/35BG

steel fibers. The results of the material compression test for 150 mm cubes are presented in Table 1.

# 2.2 | Instrumentation

In this study, the fiber optic cable BRUsens V9 from Solifos, including an external polymeric outer jacket with a rough surface, was used. The V9 cable has a 3.2 mm diameter and its minimum bending radius, when tensioned, is about 56 mm, which makes it stiffer and more suitable for surface applications than other cables without a protective jacket, such as the 125 µm-thick polyimide-coated fibers used in several previous studies, see for example. 1-4,14,26 Conversely, the V9 cable can be easily handled and deployed without risk of rupture, making it especially suitable for embedding in concrete and post-casting applications. Furthermore, a recent study by the authors showed that jacketed cables are less sensitive to local disturbances and, thus, less prone to yield strain reading anomalies.<sup>17</sup> Although the layered design of the sensor can lead to shear lag in the strain transfer between layers, thereby resulting in a certain strain attenuation between the fiber core and the substrate material, several research works have shown that the evaluation of cracks and other structural parameters is not affected provided proper calculation methods are used. 16,17

As depicted in Figures 2a, b and 3a, b, for sectional and longitudinal arrangements, all four specimens were instrumented with a similar deployment of DOFS installed in a multi-layer configuration to monitor the variation of strain along the beam in the region between the supports at 5 different locations of the beam's crosssection: two cables on the top, namely "tl" and "tr," and two more at the bottom, namely "bl" and "br," on both sides of the cross-section. The measurement on both sides enabled control of symmetry in the section plane. An additional cable was arranged at approximately the midheight of the section on one side only, namely "ml." This last cable allowed confirming the plane sections remaining plane hypothesis. Furthermore, in the specimens with post-tensioning, a further cable was arranged on the top surface of the duct before casting, namely "duct," see Figure 2c.

The Optical Distributed Sensor Interrogator (ODiSI) 6000 series from Luna Inc. was used as a data acquisition

7517648, 2025, 5, Downloaded from https://onlinelibtary.wiley.com/doi/10.1002/suco.70224 by Statens Beredning, Wiley Online Library on [24/11/025]. See the Terms and Conditions (https://onlinelibtary.wiley.com/emrs-and-conditions) on Wiley Online Library for rules of use; OA articles are governed by the applicable Creative Commons License

unit. This instrument offers a strain resolution of 1 µE, a maximum strain range of ±15,000 με and a sample rate that can go up to 250 Hz depending on the gauge pitch, cable length, and number of active channels. In all tests, the largest available spatial resolution between measuring points provided by the interrogator was chosen, namely 5.2 mm. This configuration provided a combined accuracy (sensor + interrogator) of  $\pm 2 \mu \epsilon$ , whereas the sample rate was set at 1 Hz. It is worth noting a cubic Hermite polynomial interpolation with a spatial resolution of 10 mm was performed on the measured raw data before proceeding to the analysis of the results in order to reduce the data volume without compromising the accuracy.

# Test setup and loading procedure

The test was divided into two different phases. In an initial phase, the beams rested without any additional load other than their self-weight, and in the case of the posttensioned elements, also the applied force on the tendons, see Figure 3a, b left. The total duration of this stage was 160 days. In a later stage, the beams were loaded to failure in a four-point bending setup. In both stages, the supports were kept the same, that is, rollers that allowed free rotation and horizontal displacement, at 250 mm from the beam ends. Therefore, the clear span between the center of the supports was equal to 8000 mm.

In the active loading stage, the load was introduced using two actuators equipped with two movable bearing supports symmetrically placed at 3000 mm from the rollers, thus dividing the beam into three spans, that is, two shear spans of 3000 mm and a constant bending moment region of 2000 mm, see Figure 3a, b right. Loading was applied under displacement control of one of the jacks, while the other was configured to continuously follow the same force, using a closed-loop feedback system at a displacement rate of 3 mm/min.

#### 2.4 **Post-tensioning force introduction**

The post-tensioned specimens, that is, PRC and PFRC specimens, were loaded with a post-tensioning force after 7 days of concrete hardening. The load was introduced by individually tensioning the different cables up to a force of 490 and 450 kN for PRC and PFRC, respectively. Following the specifications from the anchorage system's manufacturer, the load was introduced by tensioning the cables in the prescribed order. A force-controlled hollow jack was used in order to introduce the corresponding post-tensioning forces. The load was introduced in the different cables by successive post-tensioning operations that can be seen in Figure 4a, b. After the desired load was reached at each of the tendons, the duct containing the tendons was grouted. The grouting process utilized a gravitational method, ensuring that the grout consistency was sufficiently fluid to flow from one end of the beam to the other.

#### RESULTS AND DISCUSSION 3

The results and discussion in this section pertain to the analysis of the top left ("tl") and bottom left ("bl") sensors, which hereafter will simply be referred to as top and bottom, respectively. It should be noted that due to symmetry conditions in the section and the length of the beam, similar results were obtained for the sensors on the right side, which were deployed for redundancy and validation purposes.

### 3.1 Assessment of tendon force application and instantaneous losses

In Figure 5, a direct comparison between the force introduced in the tendons during the post-tensioning process and the measured strains with the DOFS sensors at the bottom steel bar for the PFRC beam is presented. The line type in the diagram indicates the different tendons. As observed, the force measured by the load cell drops to zero for each tendon after the jack is released, whereas the recorded strain increases according to the load introduced in each tensioning operation.

From the analysis of a single tendon's tensioning operation, it is evident that the load was not introduced in one step; instead, several tensioning operations were performed until the desired load level was achieved. Examining the first tendon more closely, as shown in the detail in Figure 5, the load was applied in three steps. The corresponding strain measured at the mid crosssection of the bottom cable followed a similar pattern, showing the same number of peaks. Post-peak behavior shows a significant drop in load magnitude compared to the strain values. This is because the drop in strain corresponds to final anchor seating losses occurring during tensioning operations, while the remaining load is transferred to the beam. A similar drop is visible in each loading step for all the tensioning operations performed, which for the first tensioning operation amounted to approximately 20  $\mu\varepsilon$ .

To assess the residual force in the tendons after completing all tensioning operations, an additional analysis

17517648, 2025, 5, Downloaded from https://onlinelibrary.wiley.com/doi/10.1002/suco.70224 by Statens Beredning, Wiley Online Library on [24/11/2025]. See the Terms

on Wiley Online Library for rules of use; OA articles are governed by the applicable Creative Commons License

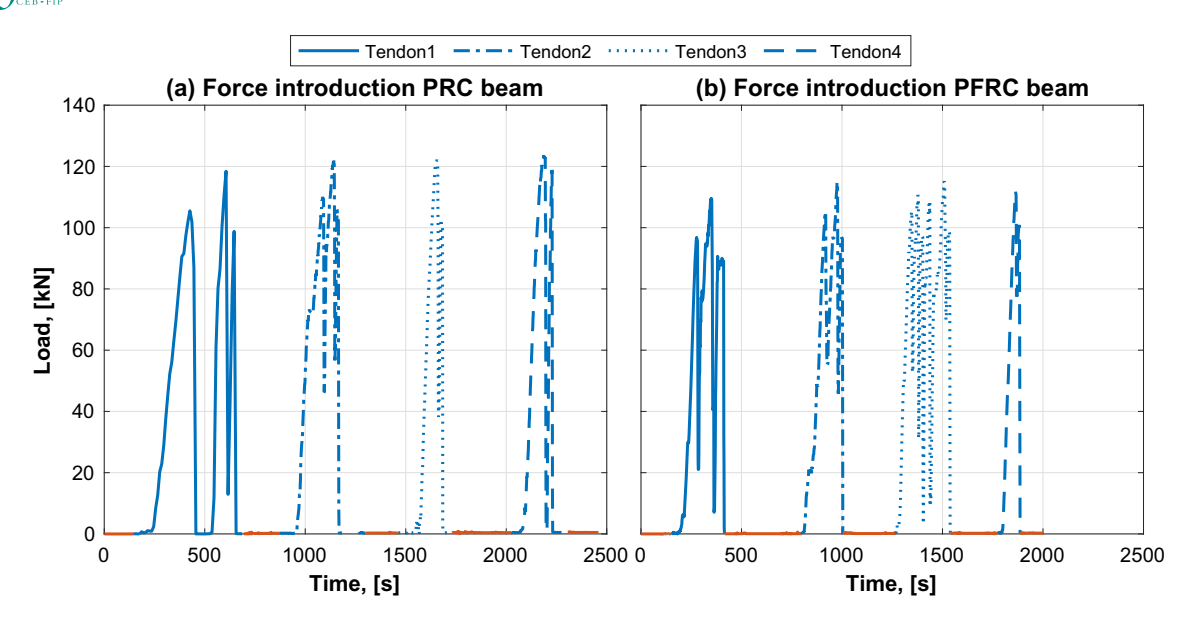


FIGURE 4 Load in the jack during the post-tensioning force introduction: (a) PRC beam and (b) PFRC beam.

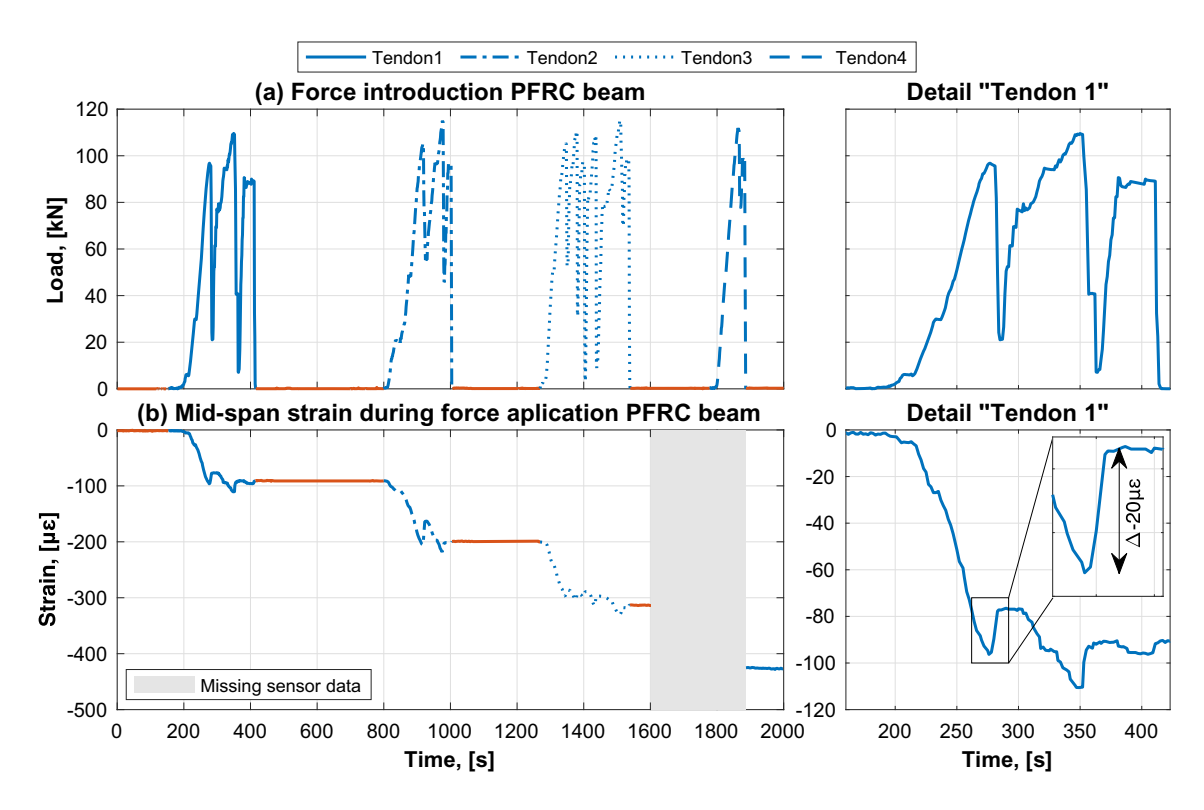


FIGURE 5 Load introduction: (a) PRC beam and (b) PFRC beam.

of the provided data was conducted. Several aspects were considered for this evaluation. First, the tendon formed a straight segment between 3000 and 5000 mm, meaning that friction losses can be neglected in that region. Consequently, any potential losses in that region can be attributed to anchor seating only. Furthermore, the frictional losses are simplified as linear within the parabolic region of the tendon, as the parabola is almost flat. Secondly, in

the absence of other external forces, the measured strains can only be attributed to the post-tensioning force. It must be noted that the effect of self-weight is not included because the DOFS sampling started after the beams were already positioned on the supports. Finally, since the position of the tendon was known, the moment related to the post-tensioning force can be expressed as in Equation (1).

$$P = \frac{M}{e},\tag{1}$$

where M represents the sectional moment, P stands for the tendon force, and e denotes the eccentricity of the tendon relative to the center of gravity of the cross-section. Additionally, it is assumed that the moment can also be determined from the section curvature in accordance with Bernoulli's beam theory, as given by Equation (2).

$$\chi = \frac{M}{FI}. (2)$$

Here, E represents the material's modulus of elasticity and I stands for the cross-section's moment of inertia. The curvature can then be calculated from the strains measured at the top and bottom of the section according to Equation (3):

$$\chi(x) = \frac{\varepsilon_{\text{bottom}}^{\text{DOFS}}(x) - \varepsilon_{\text{top}}^{\text{DOFS}}(x)}{z},$$
 (3)

where  $\varepsilon_{\mathrm{bottom}}^{\mathrm{DOFS}}(x)$  and  $\varepsilon_{\mathrm{top}}^{\mathrm{DOFS}}(x)$  are the measured strains at the bottom and top reinforcement, respectively, and z is the vertical distance between the position of the DOFS. The final assumption is that the force determined following the previous steps, when applied to the peak strain value at the mid cross-section, can be used to quantify the post-tensioning losses solely due to friction. This is because, just before the jack is released, the entire load exerted by the jack transfers to the beam, with some of it being lost due to friction between the tendon and the duct with no other losses yet occurring.

Based on the previous assumptions and examining the strain values at the straight section of the tendon, the actual force at the peak of one loading step could be computed. By comparing the calculated value to the force indicated by the load cell at the jack, the friction losses up to the start of the straight region, friction free, can be readily determined. Assuming symmetry in the tendon arrangement, losses from the end of the straight region to the passive anchor can also be estimated. Figure 6 shows in purple a quantification of these losses as a percentage, indicating how much load is lost per kN introduced. To evaluate the losses corresponding to the anchor seating, the decrease in strain after the loading step was also converted to load. It should be noted that the calculated load is not the direct loss of force due to the anchor seating as this is offset by friction in the opposite direction. Since the friction in both directions can be assumed identical, the initial loss of force at the anchor due to anchor seating and total length penetration can be estimated from

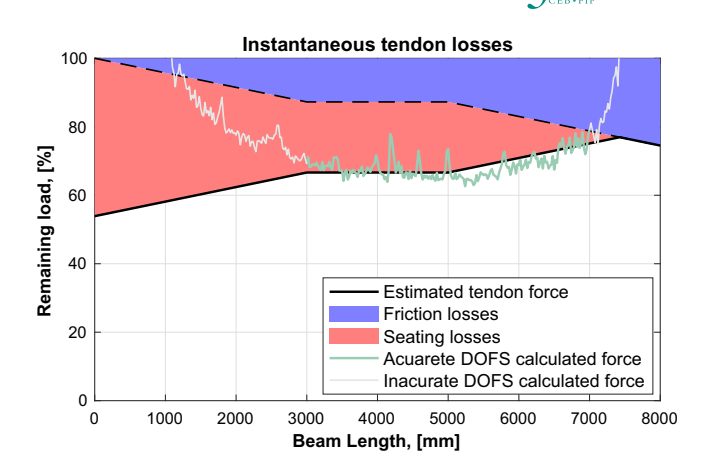


**FIGURE 6** Estimation of the instantaneous losses during tensioning of tendons.

the previously calculated values for friction losses, that is, based on the slope of the triangular area of the blue region.

Hence the seating losses are shown in Figure 6 as a shaded red area, with the final force on the tendon being the bottom envelope, indicated by a thick continuous black line. It is important to observe that when analyzing the strain values measured across different sections of the beam, the seating losses were detected further along the beam than predicted by theoretical values derived from measurements in the straight tendon region, that is, around 7500 mm; see Figure 6. This discrepancy was attributed to an overestimation in the calculation of friction losses, primarily due to slight variations in converting strain to load as a consequence of differences in geometry along the beam or actual tendon positioning that may have resulted in non-negligible discrepancies in the calculated friction losses. Since the calculation of seating losses beyond the straight region is based on the friction losses, the intersection point between them may vary within the end region. Despite some uncertainty regarding the position of the maximum load, the actual magnitude of maximum load within the tendon is not expected to show significant variations with respect to the calculated value.

It is also worth noting that a preferable method for estimating the tendon force would involve evaluating the beam's sectional forces at each coordinate along the length, instead of choosing only the straight region of the tendon. In other words, since the DOFS sensor provides strain measurements every 5 mm, theoretically it becomes possible to calculate the variation of curvature along the beam's length. By following the previously described steps and knowing the tendon's eccentricity, the remaining force in the tendon can then be estimated. However, as illustrated by the green and gray lines in

7517648, 2025, 5, Downloaded from https://onlinelibrary.wiley.com/doi/10.1002/suco.70224 by Statens Beredning, Wiley Online Library on [24/11/2025]. See the Terms and Conditions

of use; OA articles are governed by the applicable Creative Commons License

Figure 6, this approach yields inconsistent results. The inconsistency primarily stems from small errors in measuring the tendon's eccentricity when it approaches zero near the supports, which leads to significant errors in force calculation. This issue is evident in the gray lines, while the central regions, less sensitive to eccentricity variations, display good agreement when compared to calculations based solely on strain values at the beam's center.

# 3.2 | Evaluation of the time dependent effects

# 3.2.1 | Analysis of DOFS strains

As previously discussed, in the initial phase the beams were only subjected to their own self-weight and, two of them, to the post-tensioning force. Figure 7a-d depicts the strain progression measured with the DOFS at the

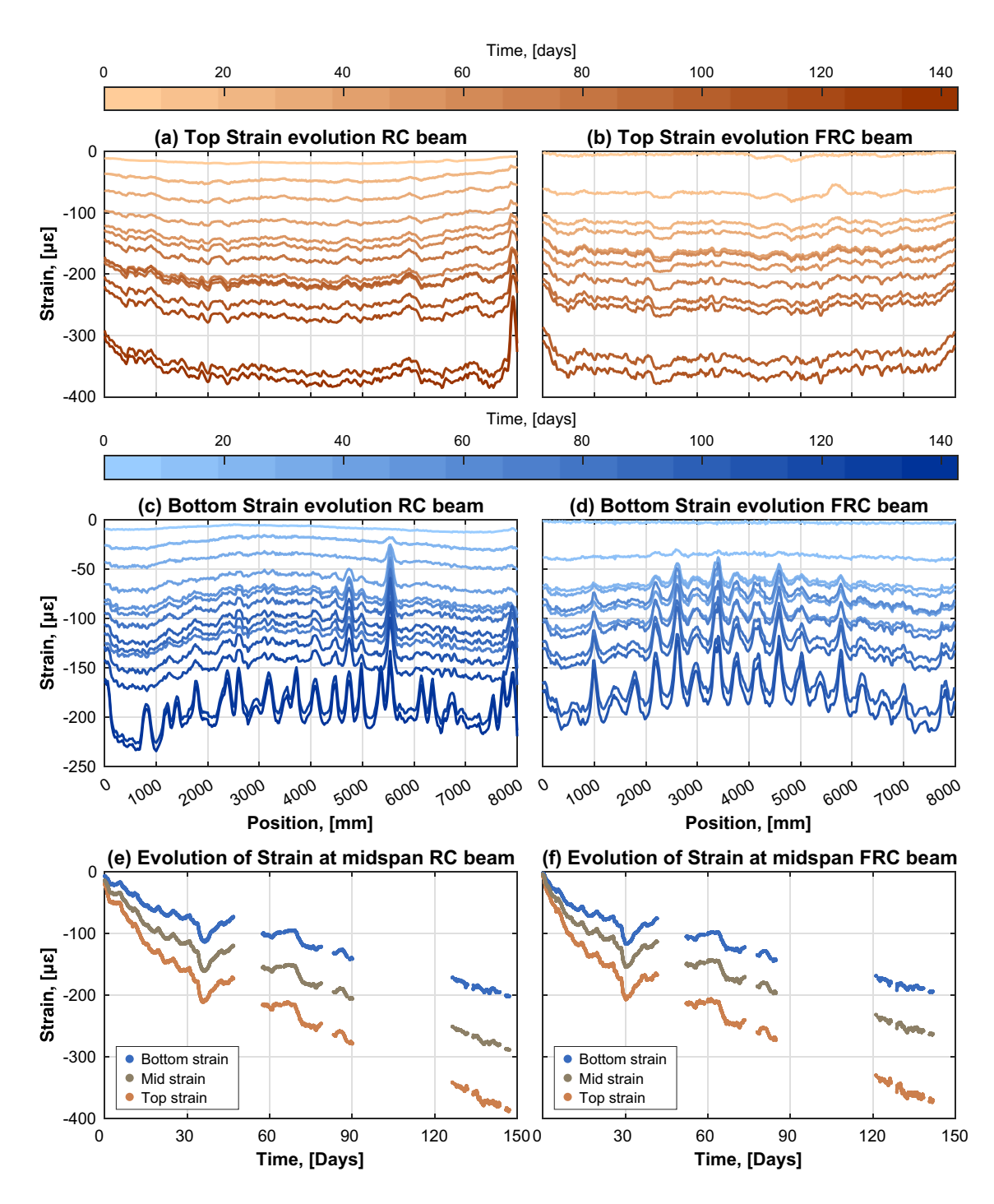


FIGURE 7 Evolution of strains top (a), (b) and bottom sensors (c), (d). (e) and (f) evolution of top, mid, and bottom strains at mid-span. RC and FRC specimens.

17517648, 2025, 5, Downloaded from https://onlinelibrary.wiley.com/doi/10.1002/suco.70224 by Statens Beredning, Wiley Online Library on [24/11/2025]. See the Terms and Conditions (https://onlinelibrary.wiley.com/terms -and-conditions) on Wiley Online Library for rules of use; OA articles are governed by the applicable Creative Commons License

different positions over time for both RC and FRC reference specimens. The results, which displayed a symmetric behavior with no significant differences between both sides, revealed that all the concrete sections throughout the beams exhibited negative strains. These strains increased quicker during the first days after casting and slowed down as the time progressed, showing a change in trend at around 10-15 days, see Figure 7e, f. This behavior was primarily ascribed to shrinkage, considering that measurements started immediately after casting when most of the shrinkage typically occurs.

Additionally, strains were observed to develop faster on the beam's top than on the bottom. This variation may have arisen due to a combination of factors. First, the T-section design may have led to differential shrinkage due to uneven drying of concrete at the top and bottom. Second, measured strain due to shrinkage is also influenced by the internal restraint caused by the steel reinforcement ratio. With more reinforcement at the bottom, shrinkage induces a positive curvature and, hence, a greater negative strain at the top. Lastly is the effect of creep due to the stresses originating from the self-weight. As a load-dependent response, creep produces positive stress-dependent strains on the lower side and negative stress-dependent strains on the top. Figure 7e, f offers a clearer view of strain changes over time for cables at the top, mid, and bottom sections, for the mid-span crosssection, highlighting all previously mentioned effects.

A closer examination of Figure 7c, d shows that localized strain peaks begin to appear when the average strain along the beam reaches approximately -100 to  $-150 \mu \epsilon$ , becoming more pronounced at around  $-200 \mu\epsilon$ . These peaks are interpreted as signs of shrinkage-induced restraint cracking. However, the cracks do not propagate through the entire specimen, since the internal restraint caused by the reinforcement is very localized to the outermost regions of the section where most of the longitudinal reinforcement is gathered. Additionally, based on the same data, unlike in Figure 7a, b where strain readings are more consistent across the beams, it can be observed that at the bottom, FRC specimens exhibit a slightly lower strain reading. This finding appears to contradict the initial geometrical assumptions since the FRC specimen is smaller than its RC counterpart, suggesting that strains due to non-mechanical phenomena under comparable environmental and external conditions should be less. However, this reduction of strains may be attributed to the incorporation of steel fibers within the FRC specimens, which, when activated after cracking, results in a distributed restraint contributing to lesser deformation of the sample.

Regarding post-tensioned samples, similar findings to those shown in Figure 7 were obtained, where the strain values between beams are similar and the general trend of the strains is to grow negative. However, from the strain measurements for both PRC and PFRC beams over the same timeframe depicted in Figure 8a-f, a significant difference in strain shapes is observed, which can be attributed to the applied external tendon forces. As derived from Figure 8a-d, shrinkage strains persist dominant, resulting in an overall negative value for stressindependent strains. Nevertheless, the stress from the post-tensioning tendons, which induces a negative bending moment in the beam, partially compensates for those strains due to creep strains. This is particularly evident for the top readings in the midspan section where nonpost-tensioned beams showed a maximum negative strain variation of about 400  $\mu\varepsilon$  at the end of the period, whereas the PRC specimens exhibited less than half that

It is also interesting to note how the non-linear profile of the tendon affects the introduced moment based on the varying lever arm of the same. Examining the strain at the top and bottom reinforcement in Figure 8a-d near the ends of the beam where the cable is centrally located, strain values similar to the non-post-tensioned elements are observed, suggesting a lower impact of direct mechanical strains from load, averaging around  $-100 \ \mu \varepsilon$ . Thus, the collected data allows for a preliminary estimate of tendon placement by comparing the two sets. In Figure 8c, d, a detailed analysis reveals higher strain values in the PFRC specimen, contrasting with the earlier assessments of the PRC specimen. This difference is wellaccounted for by the influence of the tendon-induced moment, which has an impact on strain measurements dependent on the cross-section's height, through the sectional inertia. Here, having a smaller cross-section clearly impacts and magnifies the strain results.

# 3.2.2 | Assessment of time-dependent tendon losses

Based on the results presented in the previous section, further analysis can be conducted to evaluate the loss of force in the tendons over time due to creep and shrinkage acting on the beam. Assuming full deformation compatibility between the concrete and the reinforcement, the direct value of the measured strain from the DOFS sensor attached to the duct can be used, see Figure 9a. However, this approach requires the installation of an additional cable, which may not be feasible in all cases. An alternative approach that should provide a reasonably accurate approximation of the strain value at the duct is direct interpolation assuming plane deformation of the section. Therefore, using the obtained curvature calculated by

7517648, 2025, 5, Downloaded from https://onlinelibrary.wiley.com/doi/10.1002/suco.70224 by Statens Beredning, Wiley Online Library on [24/11/2025]. See the Terms

on Wiley Online Library for rules

of use; OA articles are governed by the applicable Creative Commons License

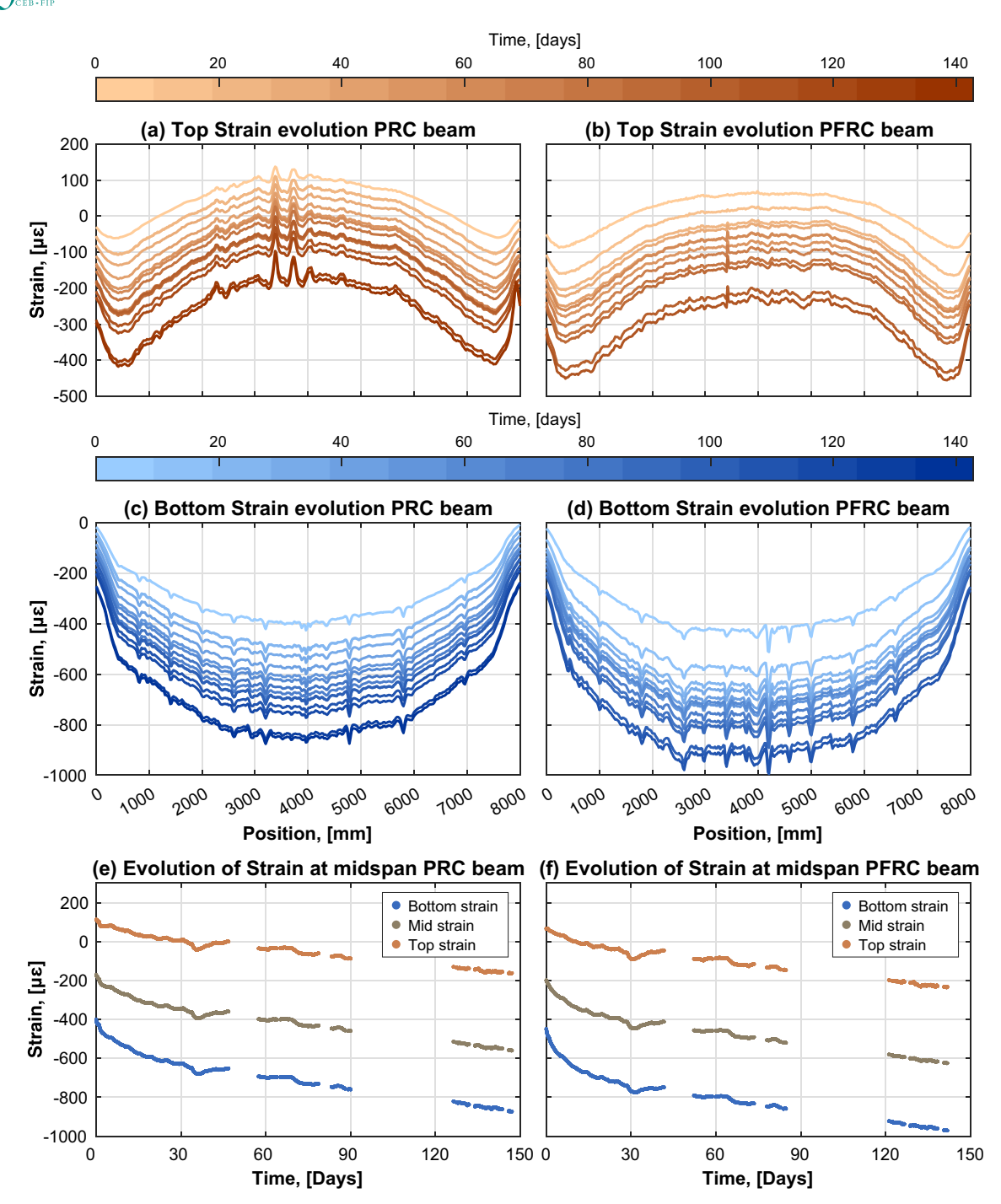


FIGURE 8 Evolution of strains top (a), (b) and bottom sensors (c), (d). (e) and (f) evolution of top, mid, and bottom strains at mid-span. PRC and PFRC specimens.

Equation (3) and the strain values at the top and bottom of the section, it is possible to estimate the strain value at the duct position as illustrated in Figure 9b. If these strain values are multiplied by the steel area and the corresponding modulus of elasticity, then an estimation of the force loss over time can be calculated. Figure 9c illustrates the force reduction at the mid-span section using both approaches. Both methods yielded good estimations of the load and were very similar to each other, although

the interpolated values were slightly less conservative than the actual values measured from the DOFS at the duct.

# 3.2.3 | Assessment of beam deflections

In this work, deflections were calculated through the double integration of the curvatures as defined by

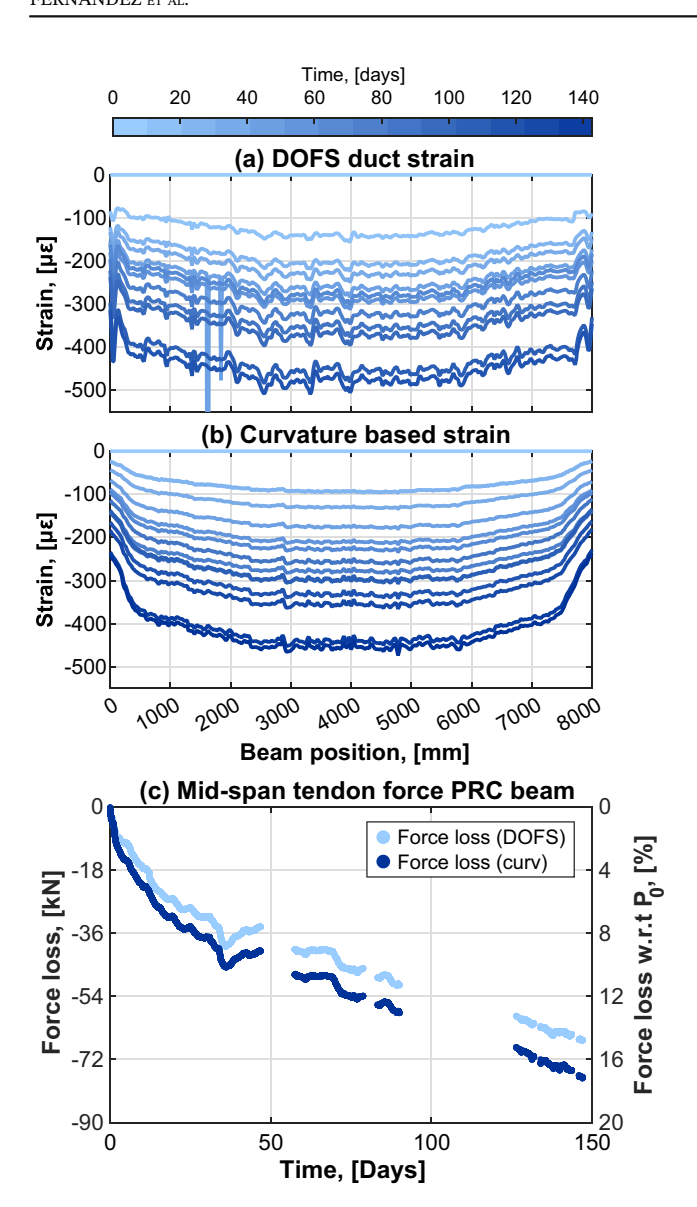


**FIGURE 9** Strain values from DOFS (a) measured at the duct, (b) calculated from the curvature. (c) Force loss in time at the midspan section.

Equation (3). This method has been presented in several studies for different types of sensors, always showing very accurate results when validated against complementary measuring systems, cf.<sup>27–29</sup> Figure 10 shows the calculated deflection for the four specimens with respect to time. The RC and FRC specimens exhibit negative values of deflection, indicating downward deformation. This deflection does not include the deflection of the self-weight, as the measurements were started after the specimen's placement. Consequently, the increase in downward deflection corresponds to the resultant effects of creep and shrinkage occurring concurrently. The mid-span deflection exhibits the typical behavior of creep. However, the deflection did not converge toward an asymptotic value as quickly as it

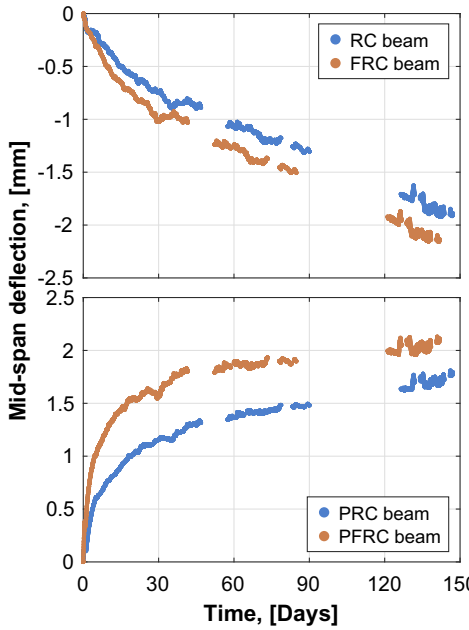


**FIGURE 10** Comparison of deflections computed by DOFS strains in time.

would be expected, which was attributed to the combined effects of creep and differential shrinkage at the section due to the T-shape section, causing a positive curvature in the section.

When analyzing post-tensioned specimens, it can be observed that the DOFS sensors enable a good characterization of the deflection, which in this case is a positive deflection indicating an uplift of the beam. Similarly to the reference specimens, only the time-dependent component of the deflection is shown, meaning that the elastic deformation due to the introduction of the posttensioning load in the elements is also subtracted. This deflection was similar for both specimens, that is, PRC and PFRC, and calculated to be around 4.8 mm, consistent with the applied load and the specific specimen height. However, as shown in Figure 10, the rate of deflection increase due to creep over time is larger in the PFRC specimen. This also aligns with previous observations, where the lower height and consequently the higher stress levels in the section are the main reasons for the increased creep-induced deflection.

# 3.3 | Analysis of the specimens under load

# 3.3.1 | Crack detection and crack evaluation

The long-term integrity of RC concrete structures in general, and post-tensioned structures in particular, where a

17517648, 2025, 5, Downloaded from https://onlinelibrary.wiley.com/doi/10.1002/succ.70224 by Statens Beredning, Wiley Online Library on [24/11/2025]. See the Terms and Conditional Conditions of the Conditional Conditional Conditions of the Conditional Condit

conditions) on Wiley Online Library for rules of use; OA articles are governed by the applicable Creative Commons License

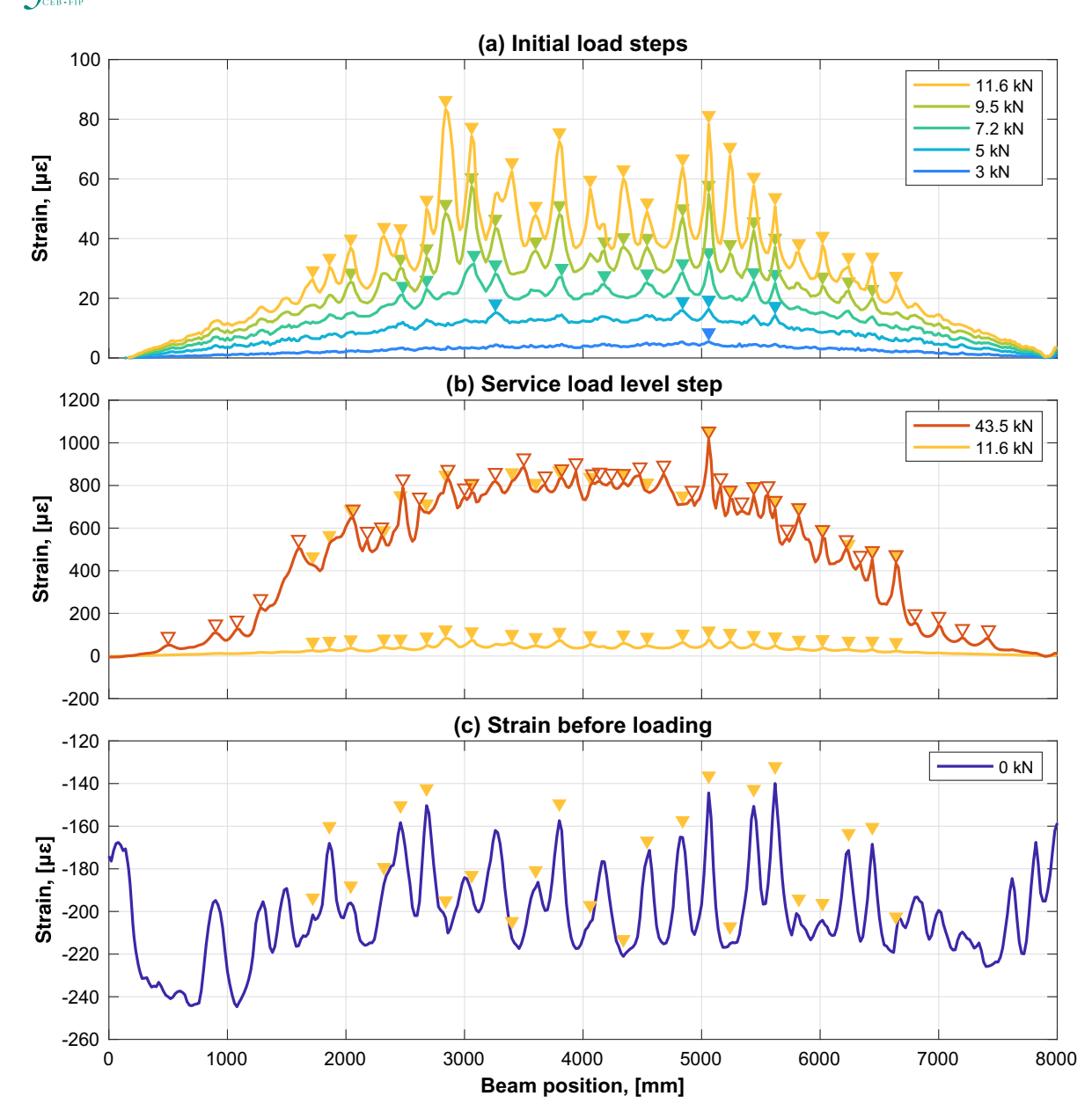


FIGURE 11 (a), (b) Detection of cracking from strain profiles at different load levels, (c) cracks detected under loading compared to the strains on the last stage of the long-term test. RC specimen.

failure of the tendon may lead to a very brittle and catastrophic collapse, is known to be particularly sensitive to cracking as this may lead to the initiation of degradation processes. Therefore, an important aspect of any monitoring system for post-tensioned structures is its capability of detecting cracking onset and crack propagation, at least under service loads. Therefore, in this work the ability of detecting cracks by the DOFS was also studied in detail.

Figure 11a-c shows the measured strain at the bottom bar under the initial loading steps. As it can be seen in Figure 11a the crack detection algorithm used was able to capture the first crack at a very early load stage, being the strain measured at the peak around  $8 \mu \varepsilon$ . Further, the following load steps lead to more cracks that are subsequently detected by the same algorithm. When comparing the last load step presented in Figure 11a to a load level equivalent to the service loads, see Figure 11b, it can be seen that the crack positions detected are mostly still captured, even detecting new developed cracks. It must be noted that, the strain values shown in Figure 11a, b corresponds to the mechanical strain consequence of the applied load only, meaning that any previous existing strain is not included. When comparing the cracks detected at the last load step in Figure 11a to the initial strain value right before any load is introduced,

17517648, 2025, 5, Downloaded from https://onlinelibrary.wiley.com/doi/10.1002/suco.70224 by Statens Beredning, Wiley Online Library on [24/11/2025]. See the Terms and Conditions

conditions) on Wiley Online Library for rules of use; OA articles are governed by the applicable Creative Commons License

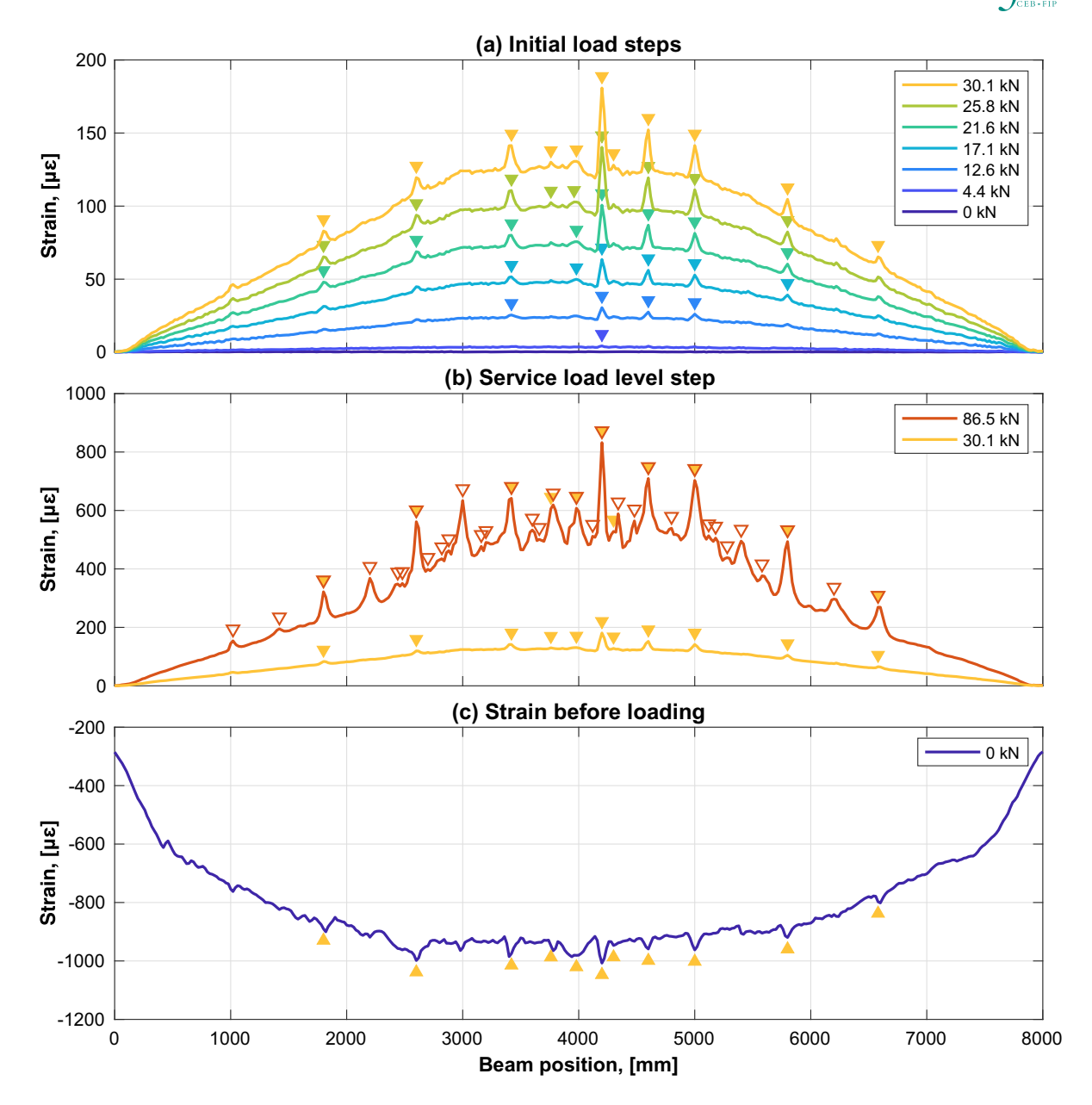


FIGURE 12 (a), (b) Detection of cracking from strain profiles at different load levels, (c) cracks detected under loading compared to the strains on the last stage of the long-term test. PFRC specimen.

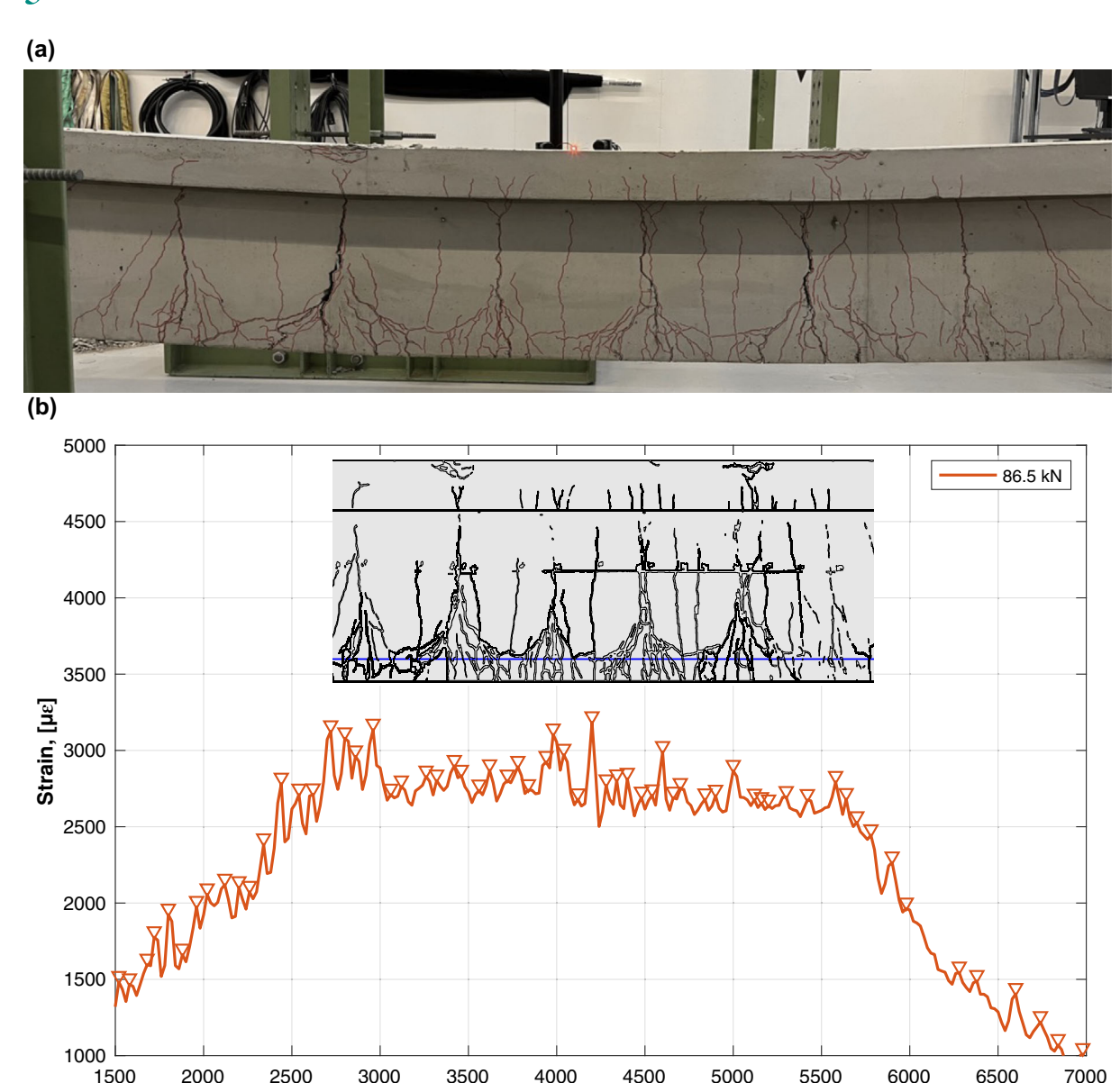
it is clear that such cracks, largely coincide with the strain peaks. As described in Section 3.2.1, the RC beam developed shrinkage-induced cracking already in the initial stage, denoted by the measured peaks in the strain. Despite no additional evidence was collected beyond the strain peaks in the sensor, it still can be concluded from the comparison that at least incipient cracking occurred at these locations, later developing into full cracks.

The same analysis was carried out for the PRC and PFRC beams, both describing similar behavior. As illustrated for the PFRC specimen in Figure 12a, it can be seen that the first crack was detected at extremely low strain levels. Furthermore, it can be observed that, in

general, the number of cracks detected is fewer compared to the specimen shown in Figure 11 for the same load level. This is due to the presence of the tendon force that successfully holds the section together, delaying the crack opening. When comparing the last load step in Figure 12a to the strains captured at a serviceability load level, it could be observed that the cracks previously detected were mostly at the same positions, and new cracks developed, see Figure 12b. Again, the comparison depicted in Figure 12a, b corresponds to the mechanical strains only, due to the applied load, meaning that any previous effect was subtracted. Figure 12c plots the crack position detected in the last load step in Figure 12a over

7517648, 2025, 5, Downloaded from https://onlinelibrary.wiley.com/doi/10.1002/suco.70224 by Statens Beredning, Wiley Online Library on [24/11/2025]. See the Terms

conditions) on Wiley Online Library for rules of use; OA articles are governed by the applicable Creative Commons License



Beam position, [mm]

FIGURE 13 Crack patterns at failure for (a) PFRC beam and (b) PFRC beam with the DOFS strains.

the strain values measured right before loading, that is, at the end of the initial stage. From this figure, it can be observed that the cracks developed at positions where concentrations of compressive strains were captured. As the post-tensioned specimens could not develop cracking due to long-term effects originating from the presence of large compressive forces, a hypothesis is that those peaks, expressed as concentrations of compressive strains, corresponded to weak zones in the concrete, caused by local defects or inhomogeneities in the distribution of the material properties. As the applied load is significant, it is reasonable that weak regions surrounding the bar were already identified during the tendon post-tensioning operations. As cracking occurs likely in weakened zones

due to lower values of tensile strength or the presence of voids, the cracks most likely developed at such points. This indicates that already in the post-tensioning stage it is possible to determine where the first cracks are going to form, which, from an infrastructure maintenance perspective, is a very advantageous observation that can favor the planning of timely and preventive maintenance operations, thereby extending the structure's service life.

Lastly, Figure 13a illustrates the final crack pattern for the PFRC specimen, highlighting the impact of adding fiber reinforcement. It can be clearly seen how the fibers effectively helped distribute cracks along the beam, growing from the reinforcement and coalescing towards the main cracks, which are clearly distinguishable at the

17517648, 2025, 5, Downloaded from https://onlinelibrary.wiley.com/doi/10.1002/suco.70224 by Statens Beredning, Wiley Online Library on [24/11/2025]. See the Terms and Conditions (https://onlinelibrary.wiley.com/erms/ ) on Wiley Online Library for rules of use; OA articles are governed by the applicable Creative Commons License

webs. Additionally, Figure 13b presents a comparison between the crack pattern observed at failure and the strain profile of the bottom sensor under a high load level. Although it is challenging to align both due to the fact that the crack pattern corresponds to the failure load and the DOFS measurement from a much earlier load step (as discussed in subsequent sections, it should be noted that the DOFS ceased measuring before failure was reached), and the large number of cracks and their proximity influenced by the presence of fiber reinforcement, the agreement between both is satisfactory, with the major crack visible in both places.

### 3.3.2 Beam structural response under load

After 160 days, the beams were tested under static loading to failure to evaluate their response and the contribution of the fibers to the overall behavior. As previously shown in Figure 3, the beams were subjected to a 4-point bending configuration. Figure 14a, b shows the loaddeflection curves for the beam measured with LVDTs. As observed in Figure 14a, reference specimens exhibit typical bending failure of a reinforced concrete beam. This is indicated by a first linear elastic branch followed by yielding of the reinforcement, which in this case occurred at around 150 kN. Subsequently, the bearing capacity of the section increases slightly while the sections undergo large plastic deformations until reaching a maximum deflection of nearly 140 mm, where failure of the critical section occurred due to concrete crushing. Both RC and FRC specimens displayed similar responses, suggesting

that the contribution of the fibers was not significant for the chosen geometry and fiber dosage investigated.

Figure 14b illustrates the results for post-tensioned specimens. The first noticeable difference compared to the reference specimens is that the presence of tendons significantly delayed crack formation. A clear change in slope is observed at around 70 kN, indicating that many sections are fully cracked at this point. From there and up to around 200 kN, the beam undergoes elastic deformations, both in the concrete and the steel, until the steel starts yielding. Due to the presence of prestressing steel, which has a different material response than commonly used quenched and self-tempered reinforcement bars, the bearing capacity increases significantly after this point, reaching up to 250 kN when the section's maximum capacity is achieved. In the post-tensioned beams, failure was also caused by crushing due to high compressive stresses in the compression head. It should be noted that due to the loading conditions, where one point load was displacement-controlled while the other was matching the force applied by the first, the applied load differed between sections when compared to the deflection under the load. This behavior was observed for both series, reference and post-tensioned specimens, and was likely attributed to variations in sectional stiffness under point loads due to manufacturing differences.

The analysis of the beam plotting sectional moments at the point loads versus deflection under the jack indicates that despite applying different load displacement ratios at such, the resultant moment was in equilibrium and consistent at both locations. This confirms the symmetry in the test setup, as illustrated in Figure 15a for

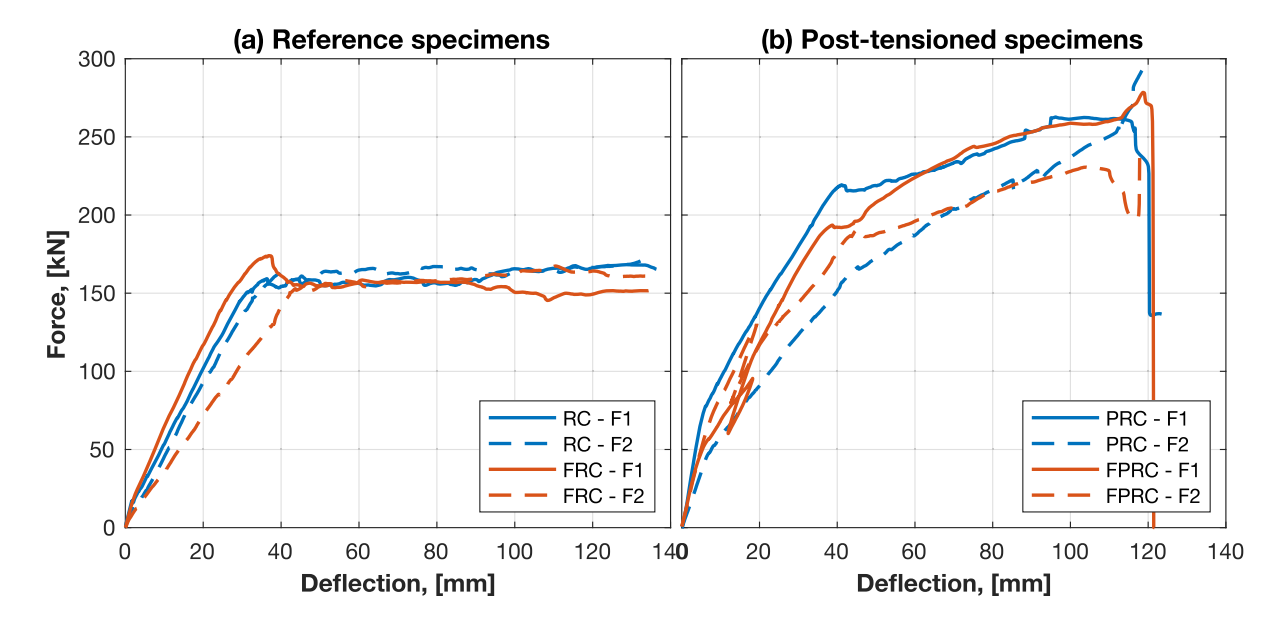


FIGURE 14 Load deflection curves for the four specimens: (a) reference specimens and (b) post-tensioned specimens.

7517648, 2025, 5, Downloaded from https://onlinelibrary.wiley.com/doi/10.1002/suco.70224 by Statens Beredning, Wiley Online Library on [24/11/2025]. See the Terms and Conditions

conditions) on Wiley Online Library for rules of use; OA articles are governed by the applicable Creative Commons License

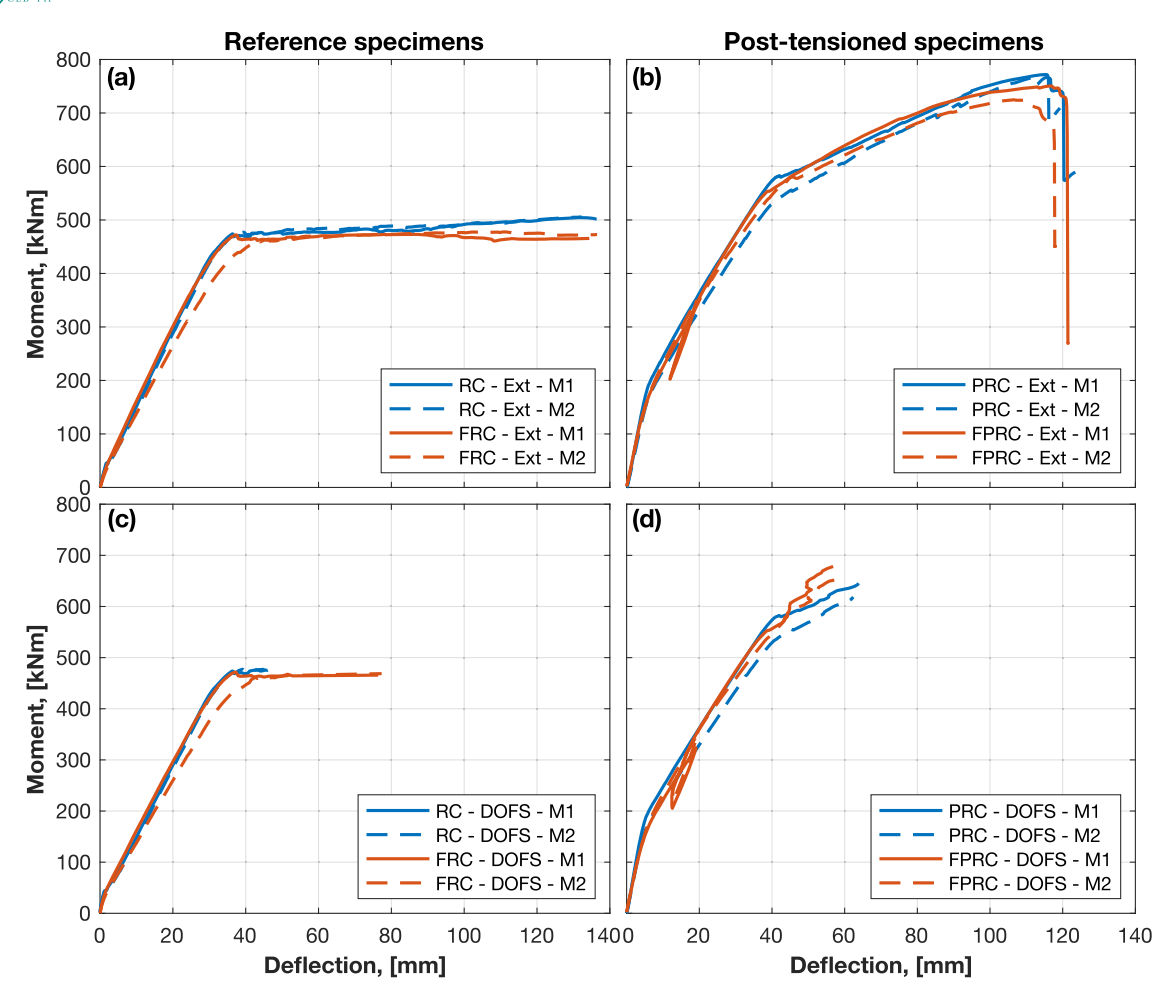


FIGURE 15 Moment deflection curves for the four specimens; (a)–(c) reference specimens, machine displacement and DOFS-calculated displacements, respectively, and (b)–(d) post-tensioned specimens, machine displacement and DOFS-calculated displacements, respectively.

reference specimens and Figure 15b for post-tensioned specimens. Similar results are presented in Figure 15c, d, which correspond to the outcomes calculated using DOFS sensors. These findings suggest that fiber optics have significant potential for accurately capturing beam response, demonstrating excellent agreement when compared with displacement transducers. However, when steel reinforcement begins to yield and large deformations are concentrated at the cracks due to substantial crack openings, the DOFS system struggles to accurately measure the strains on the cable. This can result in either inaccurate data, as depicted in Figure 15d between 45 and 60 mm of deflection, or complete loss of readings, stopping well before failure. It is important to note that even though the DOFS led to inaccurate results or data loss, the FRC specimen successfully underwent large plastic deformation before failure. This can be attributed to the capability of steel fibers to effectively control and distribute cracking, resulting in significantly smaller crack widths. This scenario is more favorable for the

DOFS system as the strain is better distributed along the cable, preventing high-strain concentrations.

# 4 | CONCLUSIONS

This study investigated the performance of jacketed DOFS based on Rayleigh backscattering for the monitoring of strains and derived structural behavior in reinforced concrete structures with and without fiber reinforcement and post-tensioning. From the results and discussion provided, the following conclusions can be drawn:

 The analysis of the DOFS strains during the tensioning operations of the tendons enabled a comprehensive assessment of the forces introduced in the element. Additionally, applying basic assumptions, a detailed evaluation of the instant losses due to both friction and seating of the anchors is possible. Directly evaluating such losses based solely on the DOFS results is, however, not recommended unless an exceptionally precise description of the tendon position is available, since minor variations in the tendon location may result in large fluctuations in the calculated force values.

- The analysis of the strains over time indicated that it is
  possible to quantify and evaluate the long-term effects,
  such as creep and shrinkage. Although these phenomena could not be decoupled, a detailed examination of
  the strain profiles revealed effects likely attributable to
  shrinkage cracking or differential shrinkage between
  the bottom and top sides of the beams.
- Additionally, by postprocessing the DOFS measurements, it was possible to monitor the beam deflection over time and assess critical aspects in post-tensioned structures, including the counter deflection caused by the tendon force and its eccentricity.
- The same strain analysis allows for the evaluation of deferred tendon losses. By using a DOFS cable directly attached to the duct, the losses at the tendon can be calculated by applying the material properties of steel and its corresponding area. Alternatively, the strain at the duct can be determined through direct interpolation, assuming a plane deformation from top and bottom sensors. However, this calculation is highly sensitive to the theoretical location of the duct, which requires accurate characterization. Any uncertainties in the duct's position will result in uncertainties in the force loss estimation.
- The analysis of the data under load revealed that DOFS is among the most recommended measurement solutions for characterizing and monitoring crack development. It was demonstrated that fiber optics, along with a good crack detection algorithm, successfully identified potential cracks with a strain concentration as low as  $8~\mu \varepsilon$ .
- A clear correlation can be observed between negative peaks captured by the bottom sensor after the posttensioning operation and the positive strain peaks identified under loading to failure. This finding suggests that the DOFS cable, when subjected to significant compressions, can detect weak zones along the beam length due to voids around the steel bars or nonuniform distribution of material properties that are prone to cracking. This may facilitate targeted inspections and potentially increase service life.
- The analysis of the load-deflection and momentdeflection curves indicated that DOFS can be used to accurately describe the beam response under service loads. However, the results also showed that DOFS struggle to deliver accurate results beyond yielding of the reinforcement due to significant strain concentrations at the cracks. In this context, it can be concluded

that the fiber reinforcement contributed positively by extending the range of capturable deflection, owing to its ability to control and distribute cracking more uniformly along the steel bars.

# **FUNDING INFORMATION**

The present research has been possible thanks to the SBUF: Svenska Byggbranschens Utvecklingsfond funding organization under the grant number SBUF-14134.

### CONFLICT OF INTEREST STATEMENT

The authors(s) declared no potential conflicts of interest with respect to the research, authorship, and/or publication of this article.

### DATA AVAILABILITY STATEMENT

The data used in this paper is available at the Swedish National Data Service (SND) under Creative Commons Attribution-NonCommercial-NoDerivatives 4.0 International (CC BY-NC-ND 4.0). The research data and metadata is searchable in the national research data portal Researchdata.se with DOI: https://doi.org/10.71870/phr9-3075.

### ORCID

Ignasi Fernandez https://orcid.org/0000-0003-4847-

Rasmus Rempling https://orcid.org/0000-0002-1122-7855

Carlos G. Berrocal https://orcid.org/0000-0003-4654-5498

## REFERENCES

- Nettis A, Nettis A, Ruggieri S, Uva G. Corrosion-induced fragility of existing prestressed concrete girder bridges under traffic loads. Eng Struct. 2024;314:118302. https://doi.org/10.1016/j.engstruct.2024.118302
- Anania L, Badalà A, D'Agata G. Damage and collapse mode of existing post tensioned precast concrete bridge: the case of Petrulla viaduct. Eng Struct. 2018;162:226–44. https://doi.org/10. 1016/J.ENGSTRUCT.2018.02.039
- Abdel-Jaber H, Glisic B. Monitoring of prestressing forces in prestressed concrete structures—an overview. Struct Control Health Monit. 2019;26:e2374. https://doi.org/10.1002/stc.2374
- Angélica AC, Gonzalez-Libreros J, Wang C, Capacci L, Biondini F, Elfgren L, et al. Assessment of residual prestress in existing concrete bridges: the Kalix bridge. Eng Struct. 2024; 311. https://doi.org/10.1016/j.engstruct.2024.118194
- Barrias A, Casas JR, Villalba S. Distributed optical fibre sensors in concrete structures: performance of bonding adhesives and influence of spatial resolution. Struct Control Health Monit. 2019;26:e2310. https://doi.org/10.1002/stc.2310
- Barrias A, Casas J, Villalba S. A review of distributed optical fiber sensors for civil engineering applications. Sensors. 2016; 16:748. https://doi.org/10.3390/S16050748
- Jansson A, Sjölander A, Berrocal CG, Rempling R, Fernandez I. Experimental investigation on prevalent local

6292 | file

failure mechanisms in hard rock tunnel linings using distributed optical fibre sensors. Eng Struct. 2025;333:120185. https://doi.org/10.1016/j.engstruct.2025.120185

- Monsberger CM, Lienhart W. Distributed fiber optic shape sensing along shotcrete tunnel linings: methodology, field applications, and monitoring results. J Civ Struct Health Monit. 2021;11:337–50. https://doi.org/10.1007/S13349-020-00455-8
- Barrias A, Rodriguez G, Casas JR, Villalba S. Application of distributed optical fiber sensors for the health monitoring of two real structures in Barcelona. Struct Infrastruct Eng. 2018;14: 967–85. https://doi.org/10.1080/15732479.2018.1438479
- Barrias A, Casas JR, Villalba S. SHM of reinforced concrete elements by Rayleigh backscattering DOFS. Front Built Environ. 2019;5:1–14. https://doi.org/10.3389/fbuil.2019.00030
- Rodriguez G, Casas JR, Villalba S. Cracking assessment in concrete structures by distributed optical fiber. Smart Mater Struct. 2015;24:035005. https://doi.org/10.1088/0964-1726/24/3/035005
- Brault A, Hoult NA, Greenough T, Trudeau I. Monitoring of beams in an RC building during a load test using distributed sensors. J Perform Constr Facil. 2019;33. https://doi.org/10. 1061/(ASCE)CF.1943-5509.0001250
- 13. Kalamkarov AL, Georgiades AV, Brown AW, Chhoa CY, Ferrier G, DeMerchant MD, et al. Strain measurement in a concrete beam by use of the Brillouin-scattering-based distributed fiber sensor with single-mode fibers embedded in glass fiber reinforced polymer rods and bonded to steel reinforcing bars. Appl Optics. 2002;41(24):5105–14. https://doi.org/10.1364/AO.41.005105
- Rodriguez G, Casas JR, Villalba S. Shear crack width assessment in concrete structures by 2D distributed optical fiber. Eng Struct. 2019;195:508–23. https://doi.org/10.1016/j.engstruct.2019.05.079
- Berrocal CG, Fernandez I, Bado MF, Casas JR, Rempling R. Assessment and visualization of performance indicators of reinforced concrete beams by distributed optical fibre sensing. Struct Health Monit. 2021;20:3309–26. https://doi.org/10.1177/ 1475921720984431
- 16. Fernandez I, Berrocal CG, Almfeldt S, Rempling R. Monitoring of new and existing stainless-steel reinforced concrete structures by clad distributed optical fibre sensing. Struct Health Monit. 2023;22:257–75. https://doi.org/10.1177/14759217221081149
- Berrocal CG, Fernandez I, Rempling R. Crack monitoring in reinforced concrete beams by distributed optical fiber sensors. Struct Infrastruct Eng. 2021;17:124–39. https://doi.org/10.1080/ 15732479.2020.1731558
- Fernandez I, Berrocal CG, Rempling R. Long-term performance of distributed optical fiber sensors embedded in reinforced concrete beams under sustained deflection and cyclic loading. Sensors. 2021;21(19):6338. https://doi.org/10.3390/s21196338
- Gao J, Shi B, Zhang W, Zhu H. Monitoring the stress of the posttensioning cable using fiber optic distributed strain sensor. Measurement. 2006;39:420–8. https://doi.org/10.1016/j.measurement. 2005.12.002
- Lan C, Zhou Z, Ou J. Full-scale prestress loss monitoring of damaged RC structures using distributed optical fiber sensing technology. Sensors. 2012;12:5380–94. https://doi.org/10.3390/s120505380
- 21. Huynh T-C, Kim J-T. FOS-based prestress force monitoring and temperature effect estimation in unbonded tendons of PSC girders. J Aerosp Eng. 2017;30. https://doi.org/10.1061/(asce)as. 1943-5525.0000608

- 22. Webb GT, Vardanega PJ, Hoult NA, Fidler PRA, Bennett PJ, Middleton CR. Analysis of fiber-optic strain-monitoring data from a prestressed concrete bridge. J Bridge Eng. 2017;22: 05017002. https://doi.org/10.1061/(asce)be.1943-5592.0000996
- Derkowski W, Sieńko R, Walczak R, Howiacki T, Bednarski Ł.
   DFOS measurements for strain analysis of anchorage zone in 57-year-old posttensioned precast girder using static and high-frequency approach. Struct Concr. 2021;22(6):1–3429. https://doi.org/10.1002/suco.202100002
- 24. Piątek B, Howiacki T, Siwowski T. Distributed fiber optic sensors for structural health monitoring of post-tensioned bridges, bridge maintenance, safety, management, digitalization and sustainability. In: Jensen JS, Frangopol DM, Schmidt JW, editors. Proceedings of the 12th International Conference on Bridge Maintenance, Safety and Management, IABMAS 2024; 2024. p. 912–20. https://doi.org/10.1201/9781003483755-106
- Piątek B, Howiacki T, Kulpa M, Siwowski T. Diagnostics of post-tensioned bridge girders using distributed fiber optic sensors. Proc Struct Integr. 2024;64:1581–8. https://doi.org/10. 1016/J.PROSTR.2024.09.412
- Bado MF, Casas JR, Dey A, Berrocal CG. Distributed optical fiber sensing bonding techniques performance for embedment inside reinforced concrete structures. Sensors. 2020;20:1–23. https://doi.org/10.3390/s20205788
- 27. Poldon JJ, Hoult NA, Bentz EC. Distributed sensing in large reinforced concrete shear test. ACI Struct J. 2019;116:235–45. https://doi.org/10.14359/51716765
- 28. Brault A, Hoult N. Monitoring reinforced concrete serviceability performance using fiber-optic sensors. ACI Struct J. n.d.; 116(1):57–70. https://doi.org/10.14359/51710870
- 29. Sigurdardottir DH, Stearns J, Glisic B. Error in the determination of the deformed shape of prismatic beams using the double integration of curvature. Smart Mater Struct. 2017;26:75002. https://doi.org/10.1088/1361-665X/aa73ec

## **AUTHOR BIOGRAPHIES**



**Ignasi Fernandez**, Chalmers University of Technology, Division of Structural Engineering, Göteborg, SE-41296, Sweden. Email: ignasi. fernandez@chalmers.se.



**Daniel Ekström**, WSP Sweden, Bridge and Hydraulic Design, Gothenburg, Sweden. Email: daniel. ekstrom@wsp.com.

17517648, 2025, 5, Dowlooaded from https://onlinelibrary.wiley.com/doi/10.1002/suco.70224 by Statens Beredning, Wiley Online Library on [24/11/2025]. See the Terms and Conditions (https://onlinelibrary.wiley.com/terms

and-conditions) on Wiley Online Library for rules of use; OA articles are governed by the applicable Creative Commons License

Rasmus Rempling, Chalmers University of Technology, Division of Construction Management and Engineering, Göteborg, SE-41296, Sweden; NCC Sverige AB, Drakegatan 10, Göteborg 412 50, Sweden. Email: rasmus. rempling@chalmers.se.



Carlos G. Berrocal, NCC Sverige AB, Drakegatan 10, Göteborg 412 50, Sweden. Email: carlos.gil@ chalmers.se.

How to cite this article: Fernandez I, Ekström D, Rempling R, Berrocal CG. Evaluation of post-tensioned reinforced and fiber reinforced concrete beams by using DOFS. Structural Concrete. 2025;26(5):6274-93. https://doi.org/10. 1002/suco.70224